ChemComm
Chemical Communications

Accepted Manuscript

This article can be cited before page numbers have been issued, to do this please use: T. Suzuki, Y. Hishikawa, B. Maity, Y. Nishiyama, K. Motai, Y. Hayamizu, S. Abe and T. Ueno, *Chem. Commun.*, 2026, DOI: 10.1039/D6CC02237E.




ROYAL SOCIETY OF CHEMISTRY

rsc.li/chemcomm

ChemComm

View Article Online
DOI: 10.1039/D6CC02237E

COMMUNICATION



# Design of a flexible aromatic gate to immobilize $C_{60}$ in a ferritin cage

Received 00th January 20xx,
Accepted 00th January 20xx

DOI: 10.1039/x0xx00000x

Taiga Suzuki[a], Yuki Hishikawa[a], Basudev Maity[a], Yumie Nishiyama[b], Kazunori Motai[b], Yuhei Hayamizu[b], Satoshi Abe[c], Takafumi Ueno*[a,d]

**We report a crystal structure of a ferritin cage immobilizing pristine fullerene ($C_{60}$) through molecular design of aromatic residues. Mutational studies and molecular dynamics (MD) simulations reveal that a flexible aromatic gate system is effective for $C_{60}$ immobilization.**

The rational design of protein assemblies is attracting attention as a powerful strategy in biomaterials engineering for constructing functional nanostructures with controlled architectures.[1] Structural stability and symmetry are key properties that facilitate design and engineering of protein assemblies. Protein cages are generally suitable templates that can leverage these properties, including DNA-binding proteins from starved cells (Dps),[2] ferritin,[3] small heat-shock proteins (HSP),[4] lumazine synthase (LS),[5] and encapsulin (Enc).[6] Ferritin is one of the most extensively studied protein cages. Ferritin cages exhibit high stability, retaining their cage structures at temperatures above 80°C,[7–9] across a wide range of pH (pH 2–10.5),[7,10] in various denaturants,[11] and even in 50% organic solvents.[11,12] Typical ferritins assemble into a 24-mer cage with 2-, 3-, and 4-fold symmetry (Fig. 1).[13,14] Among these interfaces, the 2-fold symmetric interface is the most stable due to strong inter-subunit interactions,[11,13] which enables the introduction of multiple mutations at this interface (Fig. 1).[9,15–18]

These properties of ferritins allow the immobilization of a broader range of molecules. The high tolerance for and efficiency of mutations in ferritins enable the rational design of diverse immobilization sites. Their compatibility with harsh environments including heat and organic solvents allows molecular complexation under such conditions,[16,19–21] thereby expanding immobilization targets to hydrophobic molecules. Despite this potential of ferritins, molecular immobilization in ferritins has been reported only for a limited range of molecules, including metal complexes,[21–23] small-molecule drugs,[24–26] and aromatic fluorescent dyes.[16] Beyond the reported targets, ferritins may also enable the immobilization of more challenging molecules, such as pristine fullerene ($C_{60}$). $C_{60}$ is particularly difficult to immobilize in proteins because of its water insolubility and bulky spherical shape (diameter of 7 Å).[27] Although crystal structures of proteins complexed with a solubility-enhanced carboxylated fullerene derivative have been reported, crystal structures of proteins that immobilize $C_{60}$ have not been reported.[28,29]

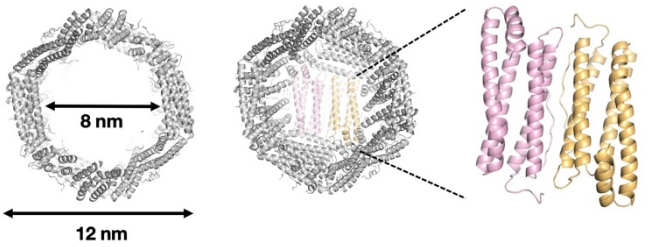


**Fig. 1** The 24-mer cage structure of a ferritin protein and its 2-fold symmetric interface (PDB: 1DAT).

In this study, we report immobilization of $C_{60}$ within a ferritin cage through molecular design. We designed a $C_{60}$ immobilization site within the ferritin cage consisting of a near-spherical hydrophobic cavity and a phenylalanine gate (Phe gate) (Fig. 2a). The X-ray crystallography and UV–vis spectroscopy confirmed that $C_{60}$ is localized at the designed immobilization site. Mutational studies and molecular dynamics (MD) simulations revealed that the flexibility of the Phe gate is essential for $C_{60}$ immobilization. The findings provide design guidelines for engineering proteins that immobilize fullerenes via non-covalent interactions.

We designed a $C_{60}$ immobilization site consisting of a near-spherical hydrophobic cavity and a Phe gate by glycine and phenylalanine substitutions, respectively (Fig. 2a). As a suitable

[a] *School of Life Science and Technology, Institute of Science Tokyo, Nagatsuta-cho 4259, Midori-ku, Yokohama 226-8501, Japan*
[b] *School of Material Science and Technology, Institute of Science Tokyo, 2-12-1, Ookayama, Meguro-ku, Tokyo 152-8550, Japan*
[c] *School of Life and Environmental Sciences, Kyoto Prefectural University, 1-5 Hangi-cho, Shimogamo, Sakyo-ku, Kyoto 606-8522, Japan*
[d] *Research Center for Autonomous Systems Materialogy (ASMat), Institute of Integrated Research, Institute of Science Tokyo, Nagatsuta-cho 4259, Midori-ku, Yokohama 226-8501, Japan*
† Electronic supplementary information (ESI) is available. See DOI: 10.1039/xxxxxxxxxx

template, we selected the 2-fold symmetric interface of recombinant horse spleen L-chain ferritin (Fr) without iron (apo-Fr), which is widely used and exhibits high structural stability among ferritin cages.[7,13] Using this as a template, we previously introduced phenylalanine mutations to immobilize aromatic fluorescent dyes via π–π stacking.[9,16] While aromatic fluorescent dyes are generally planar, $C_{60}$ is a bulky spherical molecule, which requires a different design for immobilization. For efficient uptake and immobilization of $C_{60}$, substitution with multiple aromatic amino acids[30] and a hemispherical hydrophobic cavity[28] have been suggested to be effective. Therefore, we designed a Fr mutant **apo-Fr-F3G3** (Fr-L24G/S27G/E56F/R59G/E60F/E63F). We replaced L24, S27, and R59 with Gly to create a cavity capable of accommodating $C_{60}$ (Fig. 2b). In addition, E56, E60, and E63 at the cavity entrance were replaced with Phe to form a gate (Fig. 2b). **Apo-Fr-F3G3** was expressed and purified according to a reported method,[31] and the monomeric molecular weight was confirmed by matrix-assisted laser desorption/ionization time-of-flight mass spectrometry (MALDI-TOF-MS) (Fig. S1a). The 24-mer cage assembly of **apo-Fr-F3G3** was verified by native polyacrylamide gel electrophoresis (PAGE) (Fig. S1b), and the detailed cage structure was confirmed by X-ray crystallography.

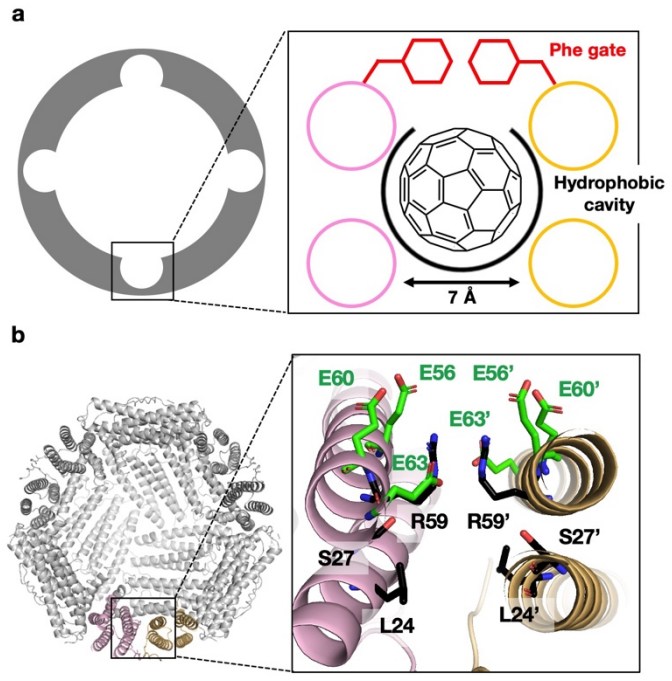


**Fig. 2** (a) Schematic representation showing the near-spherical cavities with Phe gate at the interior wall of a ferritin cage for $C_{60}$ immobilization. (b) Selected section of the 2-fold symmetric interface of apo-Fr-WT (PDB: 1DAT) showing the key residues assigned for mutation for $C_{60}$ immobilization. Selected residues for Phe and Gly mutations are shown as green and black sticks, respectively.

Complex formation of $C_{60}$ with **apo-Fr-F3G3** was performed in a mixed solvent consisting of 50% (v/v) methanol, 5% (v/v) PEG400, and 45% (v/v) buffer (50 mM Tris-HCl, 150 mM NaCl, pH 8.0 in the stock solution). The concentration of **apo-Fr-F3G3** in the reaction mixture was 10 μM, and $C_{60}$ was added in excess. The reaction mixture was sonicated for 1 h, followed by heating at 70 °C for 24 h. The reaction mixture was then subjected to dialysis against the buffer (50 mM Tris-HCl, 150 mM NaCl, pH 8.0), followed by filtration (see supporting information). The resulting complex of **apo-Fr-F3G3** with $C_{60}$ was named **$C_{60}$·Fr-F3G3** (Fig. 3a). Native PAGE confirmed that **$C_{60}$·Fr-F3G3** maintained the 24-mer cage assembly (Fig. 3b). The UV–vis spectrum of **$C_{60}$·Fr-F3G3** exhibited distinct absorption peaks at 259 and 332 nm assigned to $C_{60}$ (Fig. 3c).[32,33] Based on the absorbance of $C_{60}$ at 332 nm and the protein concentration determined by the bicinchoninic acid (BCA) assay, 2.7 ± 0.1 $C_{60}$ molecules per Fr cage were estimated, while 12 equivalent immobilization sites were designed per cage. The incomplete incorporation of $C_{60}$ is likely due to restricted access of the $C_{60}$ molecules through the channels of the Fr cage. This kinetic bottleneck may still persist due to the bulkiness of $C_{60}$, even under the harsh condition that expands the channels.[20,21] We also tested immobilization of $C_{70}$ and buckyferrocene using the same procedure. However, UV–vis spectra did not indicate the immobilization of these fullerene species, likely due to the size and shape complementarity of the hydrophobic cavity (Fig. S4). We also explored $C_{60}$ complexation with other mutants in which Phe was replaced with Tyr, Trp, or Ala (**apo-Fr-X3G3**; X = Y, W, A), but negligible absorption peaks from $C_{60}$ were observed (Fig. 3c). These results indicate that the designed cavity selectively complexes $C_{60}$, and that the Phe residues are essential for this process.

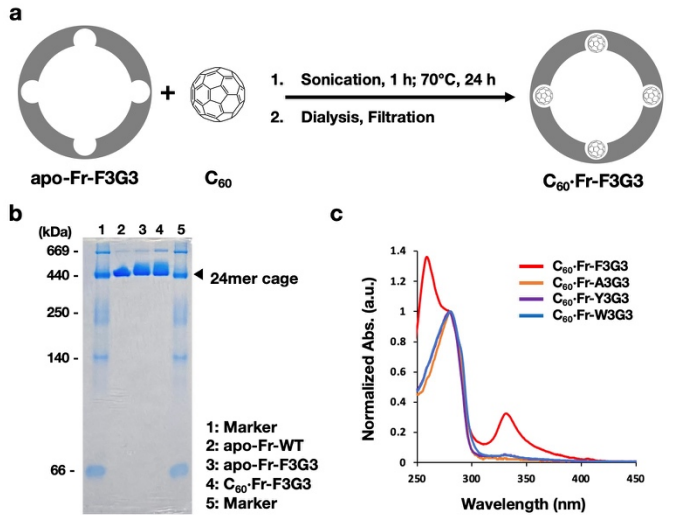


**Fig. 3** Preparation of the $C_{60}$·Fr complex and selected characterization data. (a) Schematic representation of the synthetic procedure for **$C_{60}$·Fr-F3G3**. The reaction was carried out in a solution containing 50% MeOH, 5% PEG400, 45% Buffer (50 mM Tris-HCl, 150 mM NaCl, pH 8.0). (b) Native PAGE analysis of **Fr-F3G3** before and after $C_{60}$ complexation, confirming retention of the 24-mer cage assembly. (c) UV–vis absorption spectra of various ferritin mutants complexed with $C_{60}$ (**$C_{60}$·Fr-X3G3**; X = F, Y, W, A) in aqueous buffer, showing selective complex formation only for the mutant with Phe (**$C_{60}$·Fr-F3G3**).

To obtain structural evidence of $C_{60}$ immobilization, we crystallized both **apo-Fr-F3G3** and **$C_{60}$·Fr-F3G3** and determined the X-ray structures at resolutions of 1.57 Å and 1.99 Å, respectively (Fig. 4 and Table S1 for crystallographic statistics). The structure of **apo-Fr-F3G3** showed formation of the near-spherical cavity (Fig. 4a). Both the $2F_o$-$F_c$ map in **$C_{60}$·Fr-F3G3** and the $F_o$(**$C_{60}$·Fr-F3G3**) − $F_o$(**apo-Fr-F3G3**) difference map showed a hollow quasi-spherical electron density located in the cavity (Fig.

 

View Article Online
DOI: 10.1039/D6CC02375E



S6, S7). The electron density was modeled as a $C_{60}$ molecule. Refinement yielded a partial occupancy of $C_{60}$ (0.5 per Fr dimer) which means a total of six $C_{60}$ molecules out of 12 cavities were incorporated into the 24-mer cage. Both crystal structure and BCA/absorbance analysis suggest that the designed cavities were not fully but partially filled with $C_{60}$ molecules.

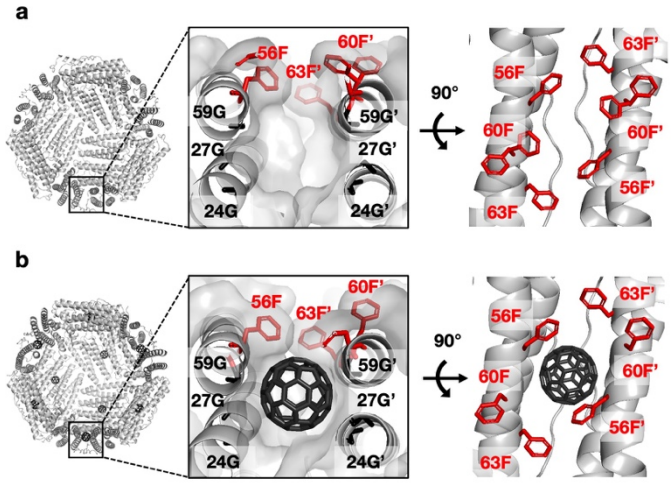


**Fig. 4** Crystal structures showing the 24-mer cage of (a) **apo-Fr-F3G3** and (b) **$C_{60}$·Fr-F3G3**. The insets show the $C_{60}$ binding site in apo form and $C_{60}$ immobilized form. The modelled $C_{60}$ molecule in **$C_{60}$·Fr-F3G3** is shown based on the electron density maps presented in Fig. S6.

The localization of $C_{60}$ in the cavity of **$C_{60}$·Fr-F3G3** was further confirmed using the environmental dependence of the UV–vis spectra of $C_{60}$.[33–36] The cavity is formed by residues 24G, 27G, Y28, L31, A55, 59G, and L81, providing a hydrophobic environment (Fig. S8a). In the crystal structure of **$C_{60}$·Fr-F3G3**, the $C_{60}$ molecule is located 3.1–4.0 Å from the nearest carbon atoms of these residues, consistent with hydrophobic interactions (Table S2).[37,38] In agreement with this, the absorption maxima (259 nm and 332 nm) suggest that $C_{60}$ is located in a hydrophobic environment similar to chloroform (Fig. S9). The absence of any shoulder peak around 450 nm excludes the possibility of $C_{60}$ aggregation (Table S3).[33,36] If $C_{60}$ were located outside the cavity, it would be exposed to a more hydrophilic environment and form aggregates with other $C_{60}$ molecules. The lack of such features supports localization of $C_{60}$ within the hydrophobic cavity.

In addition to the hydrophobic cavity, the Phe residues also contribute to providing the hydrophobic environment and the isolation of $C_{60}$. In the crystal structure of **$C_{60}$·Fr-F3G3**, the $C_{60}$ molecule is located 5.3–5.4 Å from the aromatic rings of 56F and 56F', suggesting aromatic interactions (Fig. S8b).[39] To verify the interaction between Phe and $C_{60}$, MD simulations of **apo-Fr-F3G3** and **$C_{60}$·Fr-F3G3** were performed for 100 ns using the crystal structures as initial coordinates (Movie S1 and S2). To identify the conformation of Phe residues (56F, 60F, and 63F), $\chi_1$ (N–Cα–Cβ–Cγ) dihedral angles were analysed, where 120–240° corresponds to outward orientations from the immobilization site and 240–360° corresponds to inward orientations (Fig. 5). Phe residues in **$C_{60}$·Fr-F3G3** frequently adopt inward orientations, whereas those in **apo-Fr-F3G3** exhibit flexible behaviour with both orientations (Fig. 5a). This increased probability of inward orientations suggests aromatic interactions between the Phe residues and $C_{60}$, which make the Phe side chains cover $C_{60}$ at the cavity entrance (Fig. S10a). Therefore, the Phe residues act as a gate that dynamically opens and closes in the absence of $C_{60}$, and closes upon $C_{60}$ immobilization.

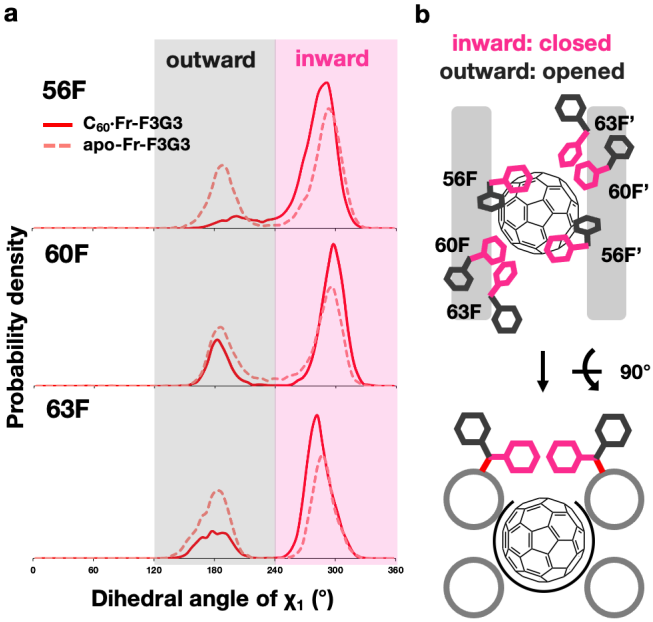


**Fig. 5** Dynamic behaviour of the Phe gate analysed by MD simulations. (a) Distributions of $\chi_1$ dihedral angles of Phe residues during 100 ns MD simulations of **$C_{60}$·Fr-F3G3** and **apo-Fr-F3G3**. (b) Representative conformations illustrating outward- and inward-oriented Phe residues at the two-fold symmetric interface relative to the immobilization site. The grey blocks represent B-helices from two subunits at the 2-fold symmetric interface. The pink sticks represent the conformer toward the $C_{60}$ molecule (inward).

To clarify the role of Phe in $C_{60}$ immobilization, we compared **Fr-F3G3** and **Fr-A3G3** (a control lacking aromatic rings in the gate residues), focusing on two processes: uptake into the cavity and retention within the cavity. Experimentally, **Fr-A3G3** does not immobilize $C_{60}$, unlike **Fr-F3G3** (Fig. 3c). For the retention process, we performed an MD simulation using an *in silico*–generated model of **$C_{60}$·Fr-A3G3**, in which the aromatic rings were deleted from the crystal structure of **$C_{60}$·Fr-F3G3**. Surprisingly, $C_{60}$ was consistently retained within the immobilization site in **$C_{60}$·Fr-A3G3** as in **$C_{60}$·Fr-F3G3** (Movie S3). Therefore, $C_{60}$ retention within the immobilization site is considered to be primarily mediated by hydrophobic interactions within the cavity, whereas the Phe residues do not appear to be essential for retention. MM/GBSA analysis also supports this interpretation, suggesting that the hydrophobic cavity accounts for most of the binding energy and is sufficient for $C_{60}$ immobilization (Fig. S11 and Table S4).[28] For the uptake process, we performed MD simulations using the crystal structures of **apo-Fr-F3G3** and **apo-Fr-A3G3**, with $C_{60}$ placed inside the cage but outside the immobilization site (**apo-Fr-F3G3 + $C_{60}$** and **apo-Fr-A3G3 + $C_{60}$**) (Fig. 4a, S12, S13). $C_{60}$ was attracted toward the vicinity of the immobilization site in **apo-Fr-F3G3 + $C_{60}$**, whereas $C_{60}$ was dispersed in **apo-Fr-A3G3 + $C_{60}$** (Movie S4, S5 and Fig. S14). Therefore, Phe residues primarily

contribute to the uptake of $C_{60}$, whereas the hydrophobic cavity governs the retention of $C_{60}$ within the immobilization site.

To clarify the factors leading to $C_{60}$ immobilization, we compared the behaviours of Phe, Tyr, and Trp gates. Experimentally, $C_{60}$ immobilization was achieved only with the Phe gate and was not observed for the Tyr or Trp gates. This behaviour does not match the reported order of binding energies between $C_{60}$ and aromatic amino acids (Trp > Tyr > Phe).[40–42] We also compared the flexibility of Phe, Tyr, and Trp residues in MD simulations of **apo-Fr-X3G3** (X = F, Y, W; Movie S2, S6, and S7). The flexibility was evaluated using the switching frequency of aromatic side chains between inward- and outward-oriented states, which correlated with the $C_{60}$ immobilization trend (Fig. 6a). Tyr residues frequently adopt outward orientations through hydrogen bonding with Arg52 and Arg64, resulting in a dispersed arrangement of aromatic rings that weakens their ability to attract $C_{60}$ (Fig. S15, S16). Regarding Trp, steric crowding caused by the bulkiness of the indole ring and inter-residue aromatic interactions restricts side-chain reorientation, limiting gate opening and $C_{60}$ access to the immobilization site (Fig. S17). In contrast, Phe residues can orient inward to form a closely positioned arrangement that attracts $C_{60}$ through multipoint aromatic interactions, and flexibly reorient to open the gate, allowing $C_{60}$ to enter the cavity (Fig. 6b, Fig. S14 and Movie S4).

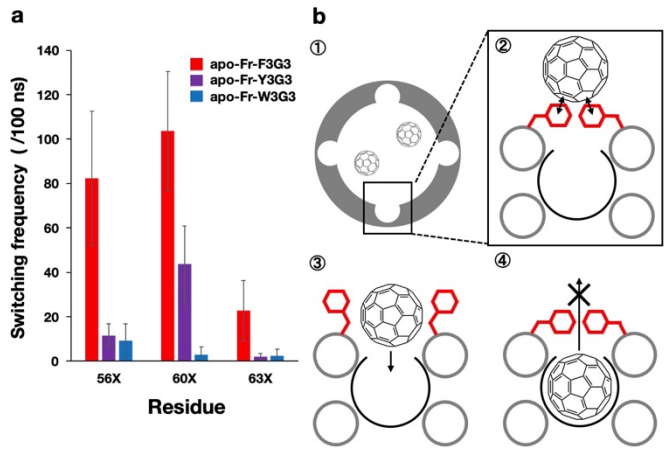


**Fig. 6** (a) Frequencies of $\chi_1$ dihedral-angle switching between inward- and outward-oriented states for residues 56X, 60X, and 63X during MD simulations of **apo-Fr-X3G3** (X = F, Y, W), reflecting differences in flexibility among Phe, Tyr, and Trp gates. (b) Proposed mechanisms of $C_{60}$ immobilization by the Phe gate.

In summary, we successfully immobilized $C_{60}$ in a Fr cage by rationally designing a near-spherical hydrophobic cavity with a Phe gate. The immobilization of $C_{60}$ in the cavity was confirmed by X-ray crystallography. We elucidated that the gate facilitates immobilization of $C_{60}$ through aromatic interactions and flexible opening and closing. This system contrasts with conventional static π-surface-based $C_{60}$ host systems,[43–46] which are difficult to realize in proteins.[47] This work provides a new and feasible design strategy for immobilizing $C_{60}$. We are continuing to engineer the Fr cage, which could provide insights into factors affecting immobilization efficiency. This approach may be extended to incorporate hydrophobic molecules into proteins for applications in drug delivery and biohybrid materials.

## Acknowledgements

View Article Online
DOI: 10.1039/D6CC02237E

This work was supported by JSPS KAKENHI Grant No. JP22H00347 to T.U. The authors thank the Facility Station Division and the Materials Analysis Division of the Research Infrastructure Management Center, Institute of Science Tokyo, for X-ray crystallographic analysis and MALDI-TOF-MS measurements, as well as the Integrative Bioscience Facility, Bioscience Center, Institute of Science Tokyo, for DNA sequence analysis. MD simulations were carried out using the TSUBAME 3.0 and 4.0 supercomputer at the Institute of Science Tokyo. The authors also thank Yutaka Matsuo for kindly providing buckyferrocene. ChatGPT (OpenAI) was used solely for language refinement.

## Conflicts of interest

The authors declare no conflict of interest.

## Data Availability Statement

All the data supporting the findings of the work are presented within the main text or supplementary information. Raw data can be availed from authors upon reasonable request. The atomic coordinates of the crystal structures have been deposited in the Protein Data Bank with the accession codes 21LO ($C_{60}$·Fr-F3G3), 21LP (apo-Fr-F3G3), 21LQ (apo-Fr-Y3G3), 21LR (apo-Fr-W3G3), 21LS (apo-Fr-A3G3).

## Author Contributions

The manuscript was written by T.S., B.M., S.A., and T.U. T.S., Y.Hi., Y.N., and K.M. performed experiments with assistance of Y.Ha. T.S., Y.Hi., and B.M. solved and refined the crystal structures. T.S. performed molecular dynamics simulations and analyzed the trajectories. T.U. supervised the project.

## References

1 J. Zhu, N. Avakyan, A. Kakkis, A. M. Hoffnagle, K. Han, Y. Li, Z. Zhang, T. S. Choi, Y. Na, C.-J. Yu and F. A. Tezcan, *Chem. Rev.*, 2021, **121**, 13701–13796.
2 R. A. Grant, D. J. Filman, S. E. Finkel, R. Kolter and J. M. Hogle, *Nat Struct Mol Biol*, 1998, **5**, 294–303.
3 D. M. Lawson, P. J. Artymiuk, S. J. Yewdall, J. M. A. Smith, J. C. Livingstone, A. Treffry, A. Luzzago, S. Levi, P. Arosio, G. Cesareni, C. D. Thomas, W. V. Shaw and P. M. Harrison, *Nature*, 1991, **349**, 541–544.
4 K. K. Kim, R. Kim and S.-H. Kim, *Nature*, 1998, **394**, 595–599.
5 K. Ritsert, R. Huber, D. Turk, R. Ladenstein, K. Schmidt-Bäse and A. Bacher, *Journal of Molecular Biology*, 1995, **253**, 151–167.
6 M. Sutter, D. Boehringer, S. Gutmann, S. Günther, D. Prangishvili, M. J. Loessner, K. O. Stetter, E. Weber-Ban and N. Ban, *Nat Struct Mol Biol*, 2008, **15**, 939–947.
7 S. Stefanini, S. Cavallo, C.-Q. Wang, P. Tataseo, P. Vecchini, A. Giartosio and E. Chiancone, *Archives of Biochemistry and Biophysics*, 1996, **325**, 58–64.
8 X. Liu, W. Jin and E. C. Theil, *Proceedings of the National Academy of Sciences*, 2003, **100**, 3653–3658.

9 Y. Hishikawa, H. Noya, S. Nagatoishi, T. Yoshidome, B. Maity, K. Tsumoto, S. Abe and T. Ueno, *Chemistry – A European Journal*, 2023, **29**, e202300488.
10 R. R. Crichton and C. F. A. Bryce, *Biochem J*, 1973, **133**, 289–299.
11 M. C. Linder, H. R. Kakavandi, P. Miller, P. L. Wirth and G. M. Nagel, *Archives of Biochemistry and Biophysics*, 1989, **269**, 485–496.
12 K. K. W. Wong, H. Cölfen, N. T. Whilton, T. Douglas and S. Mann, *Journal of Inorganic Biochemistry*, 1999, **76**, 187–195.
13 B. Gallois, B. L. d'Estaintot, M.-A. Michaux, A. Dautant, T. Granier, G. Précigoux, J.-A. Soruco, F. Roland, O. Chavas-Alba, A. Herbas and R. R. Crichton, *JBIC*, 1997, **2**, 360–367.
14 P. D. Hempstead, S. J. Yewdall, A. R. Fernie, D. M. Lawson, P. J. Artymiuk, D. W. Rice, G. C. Ford and P. M. Harrison, *Journal of Molecular Biology*, 1997, **268**, 424–448.
15 Y. Hishikawa, B. Maity, N. Ito, S. Abe, D. Lu and T. Ueno, *chem. Lett.*, 2020, **49**, 840–844.
16 Y. Hishikawa, T. Suzuki, B. Maity, H. Noya, M. Yoshizawa, A. Asanuma, Y. Katagiri, S. Abe, S. Nagatoishi, K. Tsumoto and T. Ueno, *Advanced Science*, 2025, **12**, 2417030.
17 B. Maity, J. Tian, T. Furuta, S. Abe and T. Ueno, *Crystal Growth & Design*, 2023, **23**, 7448–7458.
18 J. Tian, B. Maity, T. Furuta, T. Pan and T. Ueno, *Angewandte Chemie International Edition*, 2025, **64**, e202504608.
19 B. Jiang, X. Chen, G. Sun, X. Chen, Y. Yin, Y. Jin, Q. Mi, L. Ma, Y. Yang, X. Yan and K. Fan, *Nano Today*, 2020, **35**, 100948.
20 I. Inoue, M. Chiba, K. Ito, Y. Okamatsu, Y. Suga, Y. Kitahara, Y. Nakahara, Y. Endo, K. Takahashi, U. Tagami and N. Okamoto, *Nanoscale*, 2021, **13**, 1875–1883.
21 R. Lucignano and G. Ferraro, *Molecules*, 2024, **29**, 4045.
22 B. Maity, Y. Hishikawa, D. Lu and T. Ueno, *Polyhedron*, 2019, **172**, 104–111.
23 A. Mohanty, A. Parida, R. K. Raut and R. K. Behera, *ACS Bio Med Chem Au*, 2022, **2**, 258–281.
24 R. Liu, P. J. Loll and R. G. Eckenhoff, *The FASEB Journal*, 2005, **19**, 567–576.
25 L. S. Vedula, G. Brannigan, N. J. Economou, J. Xi, M. A. Hall, R. Liu, M. J. Rossi, W. P. Dailey, K. C. Grasty, M. L. Klein, R. G. Eckenhoff and P. J. Loll, *Journal of Biological Chemistry*, 2009, **284**, 24176–24184.
26 S. Oakley, L. S. Vedula, W. Bu, Q. C. Meng, J. Xi, R. Liu, R. G. Eckenhoff and P. J. Loll, *PLOS ONE*, 2012, **7**, e32070.
27 H. W. Kroto, J. R. Heath, S. C. O'Brien, R. F. Curl and R. E. Smalley, *Nature*, 1985, **318**, 162–163.
28 K.-H. Kim, D.-K. Ko, Y.-T. Kim, N. H. Kim, J. Paul, S.-Q. Zhang, C. B. Murray, R. Acharya, W. F. DeGrado, Y. H. Kim and G. Grigoryan, *Nat Commun*, 2016, **7**, 11429.
29 H. Benyamini, A. Shulman-Peleg, H. J. Wolfson, B. Belgorodsky, L. Fadeev and M. Gozin, *Bioconjugate Chem.*, 2006, **17**, 378–386.
30 M. Liutkus, A. López-Andarias, S. H. Mejías, J. López-Andarias, D. Gil-Carton, F. Feixas, S. Osuna, W. Matsuda, T. Sakurai, S. Seki, C. Atienza, N. Martín and A. L. Cortajarena, *Nanoscale*, 2020, **12**, 3614–3622.
31 K. Iwahori, K. Yoshizawa, M. Muraoka and I. Yamashita, *Inorg. Chem.*, 2005, **44**, 6393–6400.
32 Henry. Ajie, M. M. Alvarez, S. J. Anz, R. D. Beck, Francois. Diederich, K. Fostiropoulos, D. R. Huffman, Wolfgang. Kraetschmer, Yves. Rubin and et al., *J. Phys. Chem.*, 1990, **94**, 8630–8633.
33 T. Andersson, G. Westman, O. Wennerström and M. Sundahl, *J. Chem. Soc., Perkin Trans. 2*, 1994, 1097–1101.
34 I. Renge, *J. Phys. Chem.*, 1995, **99**, 15955–15962.
35 T. Andersson, K. Nilsson, M. Sundahl, G. Westman and O. Wennerström, *J. Chem. Soc., Chem. Commun.*, 1992, 604–606.
36 X. Chang and P. J. Vikesland, *Environ. Sci. Technol.*, 2011, **45**, 9967–9974.
37 R. F. de Freitas and M. Schapira, *MedChemComm*, 2017, **8**, 1970–1981.
38 J. Mihel, M. Šikić, S. Tomić, B. Jeren and K. Vlahoviček, *BMC Struct Biol*, 2008, **8**, 21.
39 S. K. Burley and G. A. Petsko, *Science*, 1985, **229**, 23–28.
40 A. de Leon, A. F. Jalbout and V. A. Basiuk, *Chemical Physics Letters*, 2008, **452**, 306–314.
41 V. A. Basiuk and E. González-Luciano, *Fullerenes, Nanotubes and Carbon Nanostructures*, 2016, **24**, 371–379.
42 T. D. Marforio, A. Calza, E. J. Mattioli, F. Zerbetto and M. Calvaresi, *International Journal of Molecular Sciences*, 2021, **22**, 11567.
43 T. Haino, M. Yanase and Y. Fukazawa, *Angewandte Chemie International Edition in English*, 1997, **36**, 259–260.
44 P. D. W. Boyd, M. C. Hodgson, C. E. F. Rickard, A. G. Oliver, L. Chaker, P. J. Brothers, R. D. Bolskar, F. S. Tham and C. A. Reed, *J. Am. Chem. Soc.*, 1999, **121**, 10487–10495.
45 E. M. Pérez, L. Sánchez, G. Fernández and N. Martín, *J. Am. Chem. Soc.*, 2006, **128**, 7172–7173.
46 A. Sygula, F. R. Fronczek, R. Sygula, P. W. Rabideau and M. M. Olmstead, *J. Am. Chem. Soc.*, 2007, **129**, 3842–3843.
47 F. Trozzi, T. D. Marforio, A. Bottoni, F. Zerbetto and M. Calvaresi, *Israel Journal of Chemistry*, 2017, **57**, 547–552.

View Article Online
DOI: 10.1039/D6CC02237E

## Data Availability Statement

All the data supporting the findings of the work are presented within the main text or supplementary information. Raw data can be availed from authors upon reasonable request. The atomic coordinates of the crystal structures have been deposited in the Protein Data Bank with the accession codes 21LO (C60·Fr-F3G3), 21LP (apo-Fr-F3G3), 21LQ (apo-Fr-Y3G3), 21LR (apo-Fr-W3G3), 21LS (apo-Fr-A3G3).